Electronically Coupled Uranium and Iron Oxide Heterojunctions as Efficient Water Oxidation Catalysts

Jennifer Leduc, Yakup Gönüllü, Tero-Petri Ruoko, Thomas Fischer, Leonhard Mayrhofer, Nikolai V. Tkachenko, Chung-Li Dong, Alexander Held, Michael Moseler, and Sanjay Mathur*

The most critical challenge faced in realizing a high efficiency photoelectrochemical water splitting process is the lack of suitable photoanodes enabling the transfer of four electrons involved in the complex oxygen evolution reaction (OER). Uranium oxides are efficient catalysts due to their wide range optical absorption ($E_g \approx 1.8$–3.2 eV), high photoconductivity, and multiple valence switching among uranium centers that improves the charge propagation kinetics. Herein, thin films of depleted uranium oxide (U_3O_8) are demonstrated grown via chemical vapor deposition effectively accelerate the OER in conjunction with hematite (α-Fe_2O_3) overlayers through a built-in potential at the interface. Density functional theory simulations demonstrate that the multivalence of U and Fe ions induce the adjustment of the band alignment subject to the concentration of interfacial Fe ions. In general, the equilibrium state depicts a type II band edge as the favored alignment, which improves charge-transfer processes as observed in transient and X-ray absorption (TAS and XAS) spectroscopy. The enhanced water splitting photocurrent density of the heterostructures ($J = 2.42$ mA cm^{-2}) demonstrates the unexplored potential of uranium oxide in artificial photosynthesis.

Dr. J. Leduc, Dr. Y. Gönüllü, Dr. T. Fischer, Prof. S. Mathur
Institute of Inorganic Chemistry
University of Cologne
Cologne 50939, Germany
E-mail: sanjay.mathur@uni-koeln.de
Dr. T.-P. Ruoko, N. V. Tkachenko
Laboratory of Chemistry and Bioengineering
Tampere University of Technology
Tampere FI-33720, Finland
Dr. L. Mayrhofer, Dr. A. Held, Prof. M. Moseler
Fraunhofer Institute for Mechanics of Materials (IWM)
Freiburg, Germany
Prof. C.-L. Dong
Department of Physics
Tamkang University
Tamsui, Taiwan

The ORCID identification number(s) for the author(s) of this article can be found under https://doi.org/10.1002/adfm.201905005.

1. Introduction

New semiconductor metal oxides and heterostructures capable of driving water splitting reactions by solar irradiation alone are required for a sustainable water splitting process. Whereas most transition metal oxides cannot entirely deliver the photochemical energy to split water molecules, uranium ([Rn] $5f^36d^17s^2$) oxides are efficient photoelectrocatalysts due to their absorption properties ($E_g \approx 1.8$–3.2 eV) and easy valence switching among uranium centers that additionally augment the charge separation efficiency. With their superior catalytic properties, uranium oxides derived from abundantly available depleted uranium sources offer new application opportunities to integrate uranium-based waste in a renewable energy production cycle.

In a typical nuclear fuel chain, waste containing depleted and radioactive uranium is generated, whereby enriched uranium (3-4% ^{235}U) consumed in nuclear power stations is produced via gaseous isotope separation of naturally occurring uranium (0.7% ^{235}U) in the form of UF_6.[1] This leaves large quantities of depleted UF_6 gas (several hundred thousand tons)[2] as waste material behind, which is stored in containers, since conversion to the more readily manageable solid and stable uranium oxide (U_3O_8) is an expensive process. Given its high chemical reactivity, UF_6 reacts with atmospheric moisture to produce UO_2F_2 and HF, the latter being highly toxic and responsible for accelerating the corrosion of the storage containers. Consequently, the containers need continuous replacements causing high maintenance costs. To exemplify the reutilization of depleted uranium waste, its use as semiconductor materials,[3–6] catalysts,[7–11] and CO_2 activation[12] has been discussed, which points out the critical need for a thorough re-examination of the photophysical and -chemical properties of uranium oxides.

Depleted uranium oxides are more selective and efficient in chemical transformation processes, when compared to currently used transition metal oxides and noble metals, primarily due to the valence dynamics of uranium centers situated on the surface. In addition, the appropriate bandgap energies of thermodynamically stable uranium oxides shift the absorption edge towards longer wavelengths that further enhances the overall water splitting efficiency through increased solar energy harvesting and conversion processes.[7,13–16] Yet, the application of uranium
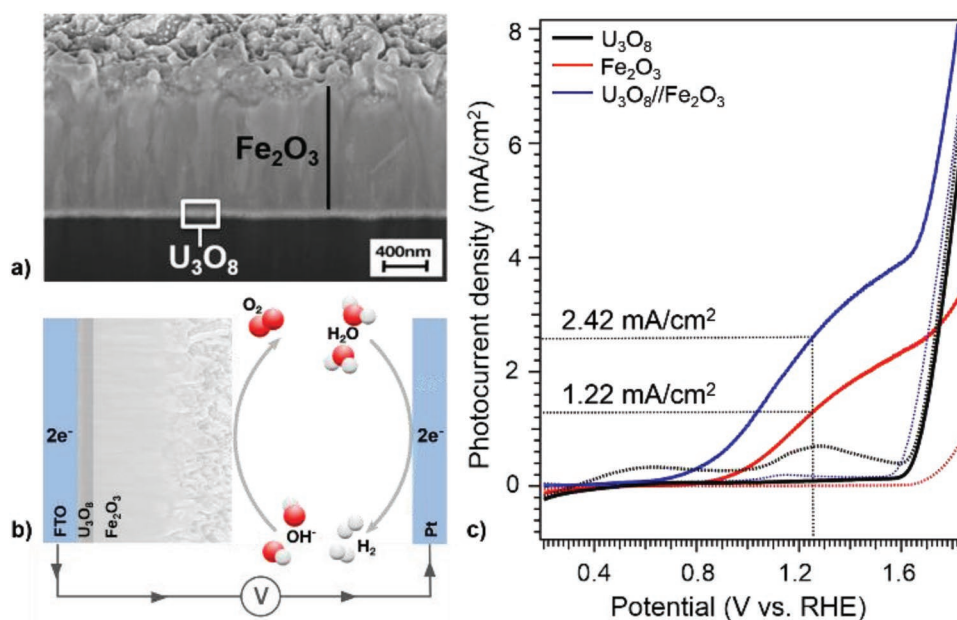
Figure 1. a) Cross-section SEM micrograph of the U_3O_8//Fe_2O_3 bilayer. b) Schematic drawing of the PEC device architecture. c) PEC measurements of bare U_3O_8, α-Fe_2O_3, and U_3O_8//Fe_2O_3 in the dark (dashed lines) and under illumination (solid lines) in 1 M NaOH electrolyte.

oxides is largely unexplored and severely limited by the difficulties in obtaining phase-pure thin films or methods enabling their immobilization on various catalytic supports.[17,18] This is mainly due to the chemical diversity in the U–O phase diagram manifesting several interconvertible stoichiometries and polymorphic modifications.[19] Herein, we report the first precisely controlled fabrication of phase-pure U_3O_8 thin films by oxygen plasma induced decomposition of the corresponding uranium precursors on diverse [silicon, fluorine-doped tin oxide (FTO), and titanium] and even large area substrates (11 × 11 cm², Figure S1, Supporting Information).[20] In addition, we demonstrate, for the first time, a high performance of U_3O_8/Fe_2O_3 bilayers (U_3O_8 coated on FTO substrate, **Figure 1**b) towards oxidation of water without the need of any sacrificial reagents or platinum-group metals as co-catalysts. Thin metal oxide underlayers (e.g., TiO_2, SiO_x, Nb_2O_5, and Ga_2O_3) have been reported to improve the water oxidation performance of ultrathin hematite layers (Table S1, Supporting Information).[21–33] This was ascribed to the structural influence of the underlayer onto the hematite layer growth and/or the suppression of the electron back injection at the hematite/substrate interface. Moreover, ZrO_2 underlayers have been reported to increase the carrier density and thus PEC performance of porous hematite photoanodes.[34] In this work, the enhanced water oxidation activity of the U_3O_8/Fe_2O_3 system in comparison to the corresponding pristine hematite photoanode originates from the higher charge carrier separation as a result of the optimal band and structural alignment in the U_3O_8/Fe_2O_3 system (**Figure 2**, and Figure S2, Supporting Information).

2. Results and Discussion

U_3O_8/Fe_2O_3 bilayers were obtained in a two-step procedure involving i) the fabrication of U_3O_8 films on FTO via plasma-assisted decomposition of the uranium (VI) precursor $[UO_2(DMOTFP)_2(DMOTFP-H)]$[20] followed by ii) deposition of hematite top layers by thermal chemical vapor deposition (CVD) of the iron source, $[Fe(OtBu)_3]_2$.[35] The crystallinity and phase purity of the U_3O_8 underlayer were confirmed by X-ray diffraction (XRD) and X-ray photoelectron spectroscopy (XPS) analyses, respectively (Figure S3, Supporting Information). The high-resolution U4f spectrum of U_3O_8 displayed the positions of the $U4f_{7/2}$ (381.4 eV) and $U4f_{5/2}$ (392.3 eV) signals to be in good agreement with reported values.[11] Recent theoretical investigations showed that in U_3O_8 the most stable arrangement consists of U^{5+}/U^{6+} (in 2:1 ratio).[36] Therefore, the satellite structure was investigated in more detail that revealed the presence of both U^{5+} and U^{6+} satellites with a binding energy difference of ≈8 and 4.8 eV to the main peaks, respectively (Figure S4, Supporting Information).[37]

In order to facilitate the charge carrier transfer from the hematite absorber layer to the FTO substrate thinner uranium oxide films (<100 nm) were deposited (Figure 1a) by adjusting the PECVD parameters. A comparative analysis of the water oxidation properties of bare α-Fe_2O_3, U_3O_8 and U_3O_8/Fe_2O_3 bilayers (Figure 1c) revealed that incorporation of a uranium oxide underlayer significantly enhanced the photoelectrochemical (PEC) properties. The buried uranium oxide layers delivered a stable PEC performance, whereas pristine uranium oxides tended to decompose in the electrolyte solutions due to high redox activity of the U_3O_8 films under alkaline conditions.[38] In comparison to the bare α-Fe_2O_3 photoanodes exhibiting a photocurrent density of 1.22 mA cm^{-2} (at 1.23 V versus RHE) and an onset potential (V_{on}) of 0.83 V, the U_3O_8/Fe_2O_3 bilayer photoanode showed a significant cathodic shift to the value of 0.62 V, which clearly demonstrated synergistic alignment of electronic states at the U_3O_8–Fe_2O_3 heterojunction. Consequently, a substantially higher photocurrent density of 2.42 mA cm^{-2} (at 1.23 V versus
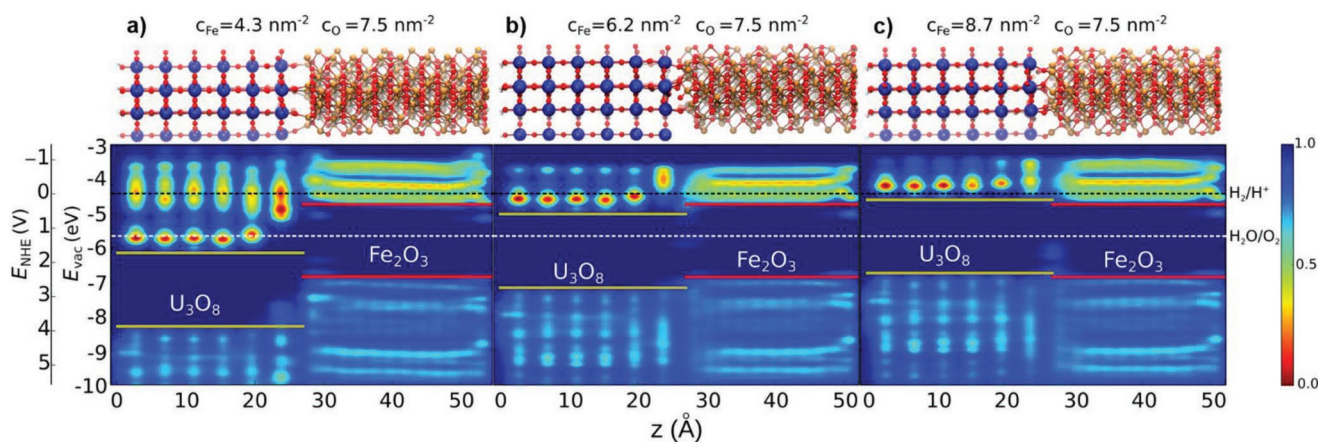
Figure 2. Localized density of states and band edge alignment at $U_3O_8//Fe_2O_3$ interfaces determined by DFT calculations for different interface Fe ion concentrations of a) $c_{Fe} = 4.3$ nm^{-2}, b) $c_{Fe} = 6.2$ nm^{-2}, and c) $c_{Fe} = 8.7$ nm^{-2}. The localized density of states is averaged over the lateral directions such that it is resolved in the direction perpendicular to the interface plane. In the atomistic structures U ions are shown in blue, Fe ions in brown, and O ions in red. The electron energy levels are given with respect to the vacuum and the normal hydrogen electrode (NHE) at pH = 0. The DFT energies were shifted such that the experimental alignment between the hematite conduction band[39,40] and the water reduction potential was retained.

RHE) was achieved in $U_3O_8//Fe_2O_3$ bilayers, which approximately corresponded to the two-fold increase in photocurrent reported for pristine α-Fe_2O_3 photoanodes. A faster transfer of photo-generated electrons from α-Fe_2O_3 to U_3O_8 in conjunction with an improved charge carrier separation is apparently due to a built-in potential at the heterojunction. This aspect was further validated by density functional theory (DFT) calculations, in situ X-ray absorption spectroscopy (XAS) and transient absorption spectroscopy (TAS) measurements.

DFT simulations were performed (Figures S5–S19 and Table S2, Supporting Information) to determine the localized density of states and calculate the relative positions of valence and conduction band edges for explicit interface models joining (001) surfaces of α-Fe_2O_3 and U_3O_8 (Figure 2). Since the band alignment of oxide heterostructures is sensitive to the detailed atomistic structure, the influence of the interfacial concentrations of O and Fe ions at the U_3O_8/Fe_2O_3 interface was systematically investigated. The calculations revealed that the band edge positions prominently depend on the amount of interfacial Fe ions, whereas the effect of O ion concentration is comparatively less pronounced.[41]

The $U_3O_8//Fe_2O_3$ heterojunction model with the lowest interfacial concentration of Fe ions was constructed by joining the α-Fe_2O_3 (001) surface terminated by a halved double layer of Fe ions with a fully O-terminated U_3O_8 (001) surface obtained by direct cleavage of the U_3O_8 bulk structure. The former is theoretically the most stable Fe_2O_3 surface over a wide range of oxygen chemical potentials.[42] In order to obtain a model for the highest investigated concentration of interfacial Fe ions, a fully O-terminated Fe_2O_3 surface and a full double layer of Fe ions at the surface was brought into contact with a cleaved U_3O_8 surface. A medium concentration of Fe ions was obtained by randomly removing 4 of 14 interfacial Fe ions per unit cell from the model for the high Fe ion concentration. Additionally, for all three cases, the concentration of interfacial O ions was varied and the thermodynamic stabilities of all investigated systems were determined as a function of the oxygen chemical potential (Figures S11–S14, Supporting Information).

The band alignments for three representative structures with a constant concentration of interfacial O ions but a varying Fe ion content (Figure 2) showed a clear trend. With an increasing concentration of interfacial Fe ions, an upward shift of Fe_2O_3 band edges ($\approx$1.44 eV) was observed, whereas the Fe_2O_3 band edges were gradually shifted downward. The interface with highest Fe ion concentration and a low O ion concentration showed a reversed band alignment with a slight offset of the Fe_2O_3 and U_3O_8 band edges (Figure 2c). This structure turned out to be thermodynamically the most stable one under reductive conditions (Figure S14, Supporting Information), whereas the structure with intermediate Fe ion concentration (Figure 2b) was apparently most stable under oxidative conditions. Hence, a type II band alignment with upshifted Fe_2O_3 band edges, which is favorable for good charge carrier separation properties can be expected under the oxidative processing conditions employed during sample fabrication. Our theoretical and experimental data indicate the deterministic role of Fe concentration in the interfacial region to adjust the band alignment in iron oxide based bilayers, particularly the here investigated $U_3O_8//Fe_2O_3$ systems. The influence of interfacial Fe ions on the band alignment is possibly due to the redox chemistry between U and Fe centers. Apparently at low Fe concentrations, all Fe ions exhibit the most stable oxidation state (+3), whereas U^{5+} and U^{6+} ions persistently co-exist in U_3O_8. The oxidation of U^{5+} upon an electronic charge transfer to the interface O-ions leads to a charge imbalance and hence to the formation of a dipole at the interface triggering the upshift of Fe_2O_3. In contrast, for high Fe ion concentrations, Fe^{2+} ions exist at the interface which can be oxidized to Fe^{3+}. This leads to a charge transfer in the opposite direction, balancing the charge transfer arising from the oxidation of U^{5+} ions and thus resulting in a reversed band alignment. The DFT results and the discussion of the band alignment using formal charge states is supported by a simple electrostatic model (Figure S18, Supporting Information).

The oxygen K-edge XAS spectra of the bilayer confirmed an increased hybridization of the O2p and Fe3d orbitals
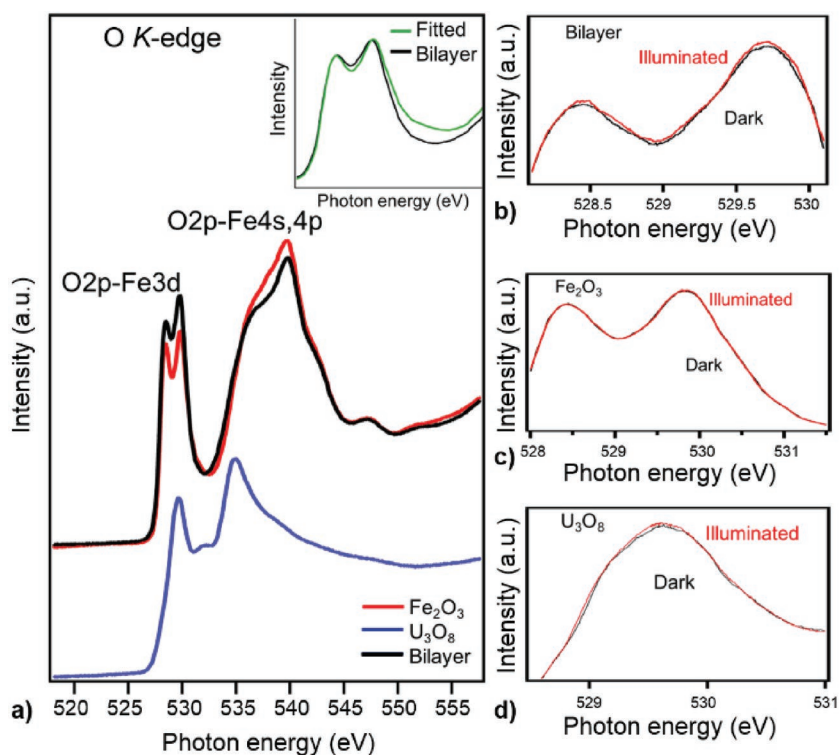
**ADVANCED
SCIENCE NEWS**
www.advancedsciencenews.com

**ADVANCED
FUNCTIONAL
MATERIALS**
www.afm-journal.de

Figure 3. XAS measurements at the O K-edge of a) bare α-Fe$_2$O$_3$, U$_3$O$_8$ and the U$_3$O$_8$//Fe$_2$O$_3$ bilayer (the inset shows the simulated and measured bilayer spectrum in the O2p-Fe3d region) and the spectral features of the b) U$_3$O$_8$/Fe$_2$O$_3$ film, c) α-Fe$_2$O$_3$ film, and d) U$_3$O$_8$ film measured in the dark and under illuminated conditions.

band alignment in the U$_3$O$_8$//Fe$_2$O$_3$ bilayer suggested by DFT calculations was verified by XAS data, which showed a significant increase in intensity in the O K-edge spectrum of the bilayer (Figure 3b). Thus, electrons generated in the α-Fe$_2$O$_3$ layer are injected into the U$_3$O$_8$ layer leaving holes in α-Fe$_2$O$_3$ that is evident in the enhanced water oxidation performance.[43] TAS performed in a ps–ns timescale elucidated the evolution of photogenerated charge carriers and their transfer and decay dynamics in the U$_3$O$_8$//Fe$_2$O$_3$ double layers (Figures S21–S28, Supporting Information).[48,49] Since U$_3$O$_8$ has negligible absorption at 425 nm (Figure S21, Supporting Information), excitation of the sample from the backside (U$_3$O$_8$) generated carriers near the U$_3$O$_8$–Fe$_2$O$_3$ interface, whereas excitation from the front side (α-Fe$_2$O$_3$) generated carriers in the bulk of hematite, mostly far from the interface.

The time-resolved spectra of the U$_3$O$_8$// Fe$_2$O$_3$ bilayer showed two spectrally distinct absorption bands centered around 460 and 550 nm (**Figure 4**a) due to a fast transfer of photogenerated electrons from the α-Fe$_2$O$_3$ into the U$_3$O$_8$ layer (460 nm) and the absorption of photo-excited electrons in the hematite layer (550 nm). A bleaching was observed for the single α-Fe$_2$O$_3$ layer at 460 nm and lower wavelengths, whereas a single U$_3$O$_8$ layer exhibited a positive absorption similar to that observed for the U$_3$O$_8$//Fe$_2$O$_3$ double layer when excited with 365 nm light (Figure 4b, and Figure S22, Supporting Information). On this timescale, the transient absorption is composed of a superposition of the absorptions of both photoexcited holes and electrons with the main component of the transient absorption decay at 700 nm constituted by recombination processes (Figure 4c).[48,49] However, the main difference with backside illumination is manifested in the faster removal of electrons from the α-Fe$_2$O$_3$ layer due to the built-in potential at the U$_3$O$_8$//Fe$_2$O$_3$ double layer. This is corroborated by a faster initial decay and smaller remaining amplitude at longer delay times as well as in the larger 0.35 ps lifetime component (Figure 4c, and Table S3, Supporting Information). The two middle decay components are nearly identical, with the difference in transient absorption that formed within the first picosecond remaining well beyond the measurement timescale (component with lifetime over 10 ns). Upon front side illumination, the transient absorption decay at 460 nm was relatively slow with about 50% of the signal amplitude remaining after 6.5 ns (Figure 4d). In comparison, 50% of the transient absorption signal decays with a lifetime of 0.35 ps upon backside illumination. This is reasonably explained by the transfer of photoexcited electrons from the α-Fe$_2$O$_3$ layer into the U$_3$O$_8$ layer with electron injection being more pronounced and more rapid when the excitation comes from the interfacial region. This illustrates the significance of the uranium oxide layer buried between the iron oxide layer and the FTO substrate.
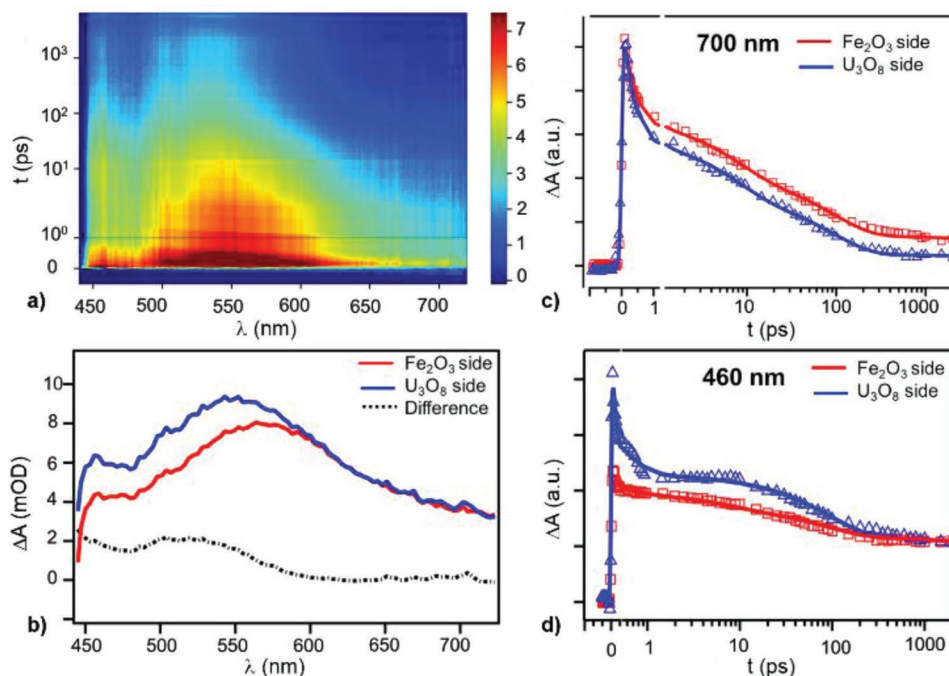
(**Figure 3**a). When compared to bare hematite photoanodes, the intensity ratio of the O2p-Fe3d relative to the O2p-Fe4s,4p feature is enhanced, which was previously reported to directly correlate with the contribution of covalent bonding in Fe$_2$O$_3$.[43,44] The increased character of the O2p states near the Fermi level promotes the injection/extraction of electrons from oxygen sites and thus increases the oxygen evolution reaction (OER) activity.[45] This in conjunction with the reported built-in potential in heterojunctions correlates well with the observed cathodic shift in the bilayered photoanodes.[46] In addition, the coherent interface originating from an Fe-terminated Fe$_2$O$_3$ (001) surface with a fully O-terminated U$_3$O$_8$ (001) is expected to reinforce the d-p overlap in hematite leading to additional electron transfer especially in view of the diffused character of the orbitals in uranium oxides. The small but significant difference is due to the fact that this change in electronic structure and stronger O2p–Fe3d hybridization mostly occurs in the interfacial region.

The in situ XAS spectra under dark and illuminated conditions (Figure 3, and Figure S20, Supporting Information) showed that in comparison to the Fe L- (Figure S20a, Supporting Information) and the O K-edge (Figure 3c) in α-Fe$_2$O$_3$, both the oxygen (K) and uranium (N) edges are photoactive in U$_3$O$_8$ (Figure 3d, and Figure S20b, Supporting Information). The high density of unoccupied states in the conduction band (O2p and U5f states) of uranium oxide promotes photo-induced charge carrier dynamics.[47] This leads to a superior conductance of charge carriers in the U$_3$O$_8$/Fe$_2$O$_3$ bilayers. The type II

Figure 4. a) Time-resolved transient absorption spectra of $U_3O_8//Fe_2O_3$ when excited from the backside (U_3O_8) with 425 nm light. The timescale was linear up to 1 ps (solid line) and logarithmic on longer delay times. The decays were corrected for chirp (group velocity dispersion). b) Time-resolved transient absorption spectra of $U_3O_8//Fe_2O_3$ at a delay of 0.2 ps when excited from the front- and backside with 425 nm light. The dashed line illustrates the difference of the spectra and the transient absorption decays of $U_3O_8//Fe_2O_3$ observed at 460 and 700 nm. c) 700 nm decays, normalized at the start of the decay and d) 460 nm decays, normalized at 1000 ps. The fits for the decays were calculated with a global four exponential decay model, shown as the solid lines, whereas the diamonds and squares represent experimental data.

3. Conclusion

Availability of new and efficient photocatalysts can give fresh impetus to alternative energy technologies enabling efficient PEC splitting of (sea) water with new photoanode materials. This work represents an alternative concept in the quest of new water oxidation photocatalysts with potential of alleviating the seemingly simple OER and hydrogen evolution reaction involved in the water splitting process. The high catalytic activity and unique electronic properties of uranium oxides as buried junctions open up new perspectives for turning vastly abundant depleted nuclear fuels (mixture of uranium oxides with surrogate oxides) into efficient catalysts for solar energy conversion. The experimental data reported here elucidate that despite the critical opinion about uranium materials, the favorable intrinsic electronic behavior and outstanding water splitting properties are promising indicators to address the challenges of solar hydrogen production.

4. Experimental Section

Synthesis of $U_3O_8//Fe_2O_3$ Bilayers: U_3O_8 films were deposited on either silicon, titanium, or FTO glass substrates (2.0 cm x 2.5 cm) via PECVD in an Ar/O_2 mixture using the uranium(VI) compound $UO_2(DMOTFP)_2(DMOTFP-H)$ 1[20] with a subsequent thermal treatment in air (600 °C, 4 h). Hematite top layers were prepared by thermal CVD using $[Fe(OtBu)_3]_2$ as reported previously[35] with an additional post-deposition annealing in air (500 °C, 5 h). The resulting $U_3O_8//Fe_2O_3$

bilayers were characterized by electron microscopy, XPS, and XRD analysis (see Supporting Information for further details).

Transient Absorption Spectroscopy: The charge transfer and decay dynamics were studied using the TAS pump-probe method. The fundamental laser pulses from a Ti:Sapphire laser (Libra F, Coherent Inc., 800 nm, ≈100 fs pulse width, repetition rate 1 kHz) were directed to an optical parametric amplifier (Topas C, Light Conversion Ltd.) to produce the desired wavelength excitation pump pulses (365 and 425 nm, attenuated to 0.5 mJ cm^{-2} with neutral density filters). The single pulse measurements were averaged 5000 times. The samples were stored in nitrogen atmosphere during measurements.

In Situ X-ray Absorption Spectroscopy: The in situ XAS measurements of O *K*-, U *N*-, and Fe $L_{2,3}$-edges were carried out in TEY mode at BL20A1 at the National Synchrotron Radiation Research Center in Taiwan. The spectra of pure α-Fe_2O_3, U_3O_8, and $U_3O_8//Fe_2O_3$ bilayers were recorded in the dark and under illumination (1.5 AM solar simulator, HAL-302, Asahi Spectra, Japan).

Photoelectrochemical Measurement: PEC measurements were performed using a three-electrode configuration in a 1.0 M NaOH aqueous solution with pristine α-Fe_2O_3, U_3O_8, and $U_3O_8//Fe_2O_3$ bilayers as the working photoanodes, SCE as the reference electrode and Pt as the counter electrode. Potentials with respect to the reversible hydrogen electrode (RHE) scale were calculated using the Nernst equation ($E_{RHE} = E_{SCE} + E^0_{SCE} + 0.059$ pH). A 0.635 cm² masked-off, sealed area of photoanodes was irradiated with a 150 W Xe lamp solar simulator through an AM 1.5G filter (Oriel).

DFT Calculations: The ab-initio DFT calculations were carried out using the projector augmented wave method[50] as implemented in the Vienna ab-initio simulations package.[51,52] Hereby, the pseudo-wave functions representing the valence electrons were described by a plane wave basis set with a cut-off energy of 400 eV. All simulations were performed within the PBE+U framework in order to improve the predicted properties of the strongly localized Fe d-electrons and U f-electrons. In agreement

with literature,[36,42,53,54] an effective U of 4 eV was employed both for the Fe d and U f orbitals. All structures were relaxed until the maximum forces were smaller than 0.02 eV Å^{-1}. Antiferromagnetic ordering was assumed both in α-Fe_2O_3 and U_3O_8. The band alignment was determined by projecting the DFT wave functions onto the atomic sites of the structure to obtain the site projected density of states (PDOS). By further averaging the PDOS over the lateral directions, a localized density of states along the z-direction perpendicular to the interface was obtained (see Supporting Information for more specific information on the computational details, the generation of the interface models and the effect of the atomistic structure on the band edge alignment at the interface).

Supporting Information

Supporting Information is available from the Wiley Online Library or from the author.

Conflict of Interest

The authors declare no conflict of interest.

[1] I. Grenthe, J. Drozdzynski, T. Fujino, T. Buck, T. E. Albrecht-Schmitt, S. F. Wolf, *The Chemistry of the Actinide and Transactinide Elements*, Springer, Netherlands, **2011**.

[2] A. K. Burrell, T. M. McCleskey, P. Shukla, H. Wang, T. Durakiewicz, D. Moore, C. Olson, J. J. Joyce, Q. Jia, *Adv. Mater.* **2007**, *19*, 3559.

[3] T. T. Meek, B. von Roedern, *Vacuum* **2008**, *83*, 226.

[4] D. Gao, Z. Zhang, L. Ding, J. Yang, Y. Li, *Nano Res.* **2015**, *8*, 546.

[5] A. M. Adamska, E. L. Bright, J. Sutcliffe, W. Liu, O. D. Payton, L. Picco, T. B. Scott, *Thin Solid Films* **2015**, *597*, 57.

[6] S. Hu, H. Li, H. Liu, P. He, X. Wang, *Small* **2015**, *11*, 2624.

[7] Z. R. Ismagilov, S. V. Lazareva, *Catal. Rev.* **2013**, *55*, 135.

[8] I. Al-Shankiti, F. Al-Otaibi, Y. Al-Salik, H. Idriss, *Top. Catal.* **2013**, *56*, 1129.

[9] Z. Sofer, O. Jankovsky, P. Simek, K. Klimova, A. Mackova, M. Pumera, *ACS Nano* **2014**, *8*, 7106.

[10] G. J. Hutchings, C. S. Heneghan, I. D. Hudson, S. H. Taylor, *Nature* **1996**, *384*, 341.

[11] H. Idriss, *Surf. Sci. Rep.* **2010**, *65*, 67.

[12] A. R. Fox, S. C. Bart, K. Meyer, C. C. Cummins, *Nature* **2008**, *455*, 341.

[13] A. P. Amrute, F. Krumeich, C. Mondelli, J. Perez-Ramirez, *Chem. Sci.* **2013**, *4*, 2209.

[14] D. P. Halter, F. W. Heinemann, J. Bachmann, K. Meyer, *Nature* **2016**, *530*, 317.

[15] B. L. Scott, J. J. Joyce, T. D. Durakiewicz, R. L. Martin, T. M. McCleskey, E. Bauer, H. Luo, Q. Jia, *Coord. Chem. Rev.* **2014**, *266–267*, 137.

[16] V. R. Choudhary, R. Jha, P. Jana, *Green Chem.* **2007**, *9*, 267.

[17] Z. R. Ismagilov, S. V. Kuntsevich, N. V. Shikina, V. V. Kuznetsov, V. A. Kerzhentsev, V. A. Ushakov, V. A. Rogov, A. I. Boronin, V. I. Zaikovsky, *Catal. Today* **2010**, *157*, 217.

[18] H. M. He, D. A. Andersson, D. D. Allred, K. D. Rector, *J. Phys. Chem. C* **2013**, *117*, 16540.

[19] L. Desgranges, G. Baldinozzi, G. Rousseau, J.-C. Nièpce, G. Calvarin, *Inorg. Chem.* **2009**, *48*, 7585.

[20] L. Appel, J. Leduc, C. L. Webster, J. W. Ziller, W. J. Evans, S. Mathur, *Angew. Chem., Int. Ed.* **2015**, *54*, 2209.

[21] L. Steier, I. Herraiz-Cardona, S. Gimenez, F. Fabregat-Santiago, J. Bisquert, S. D. Tilley, M. Gratzel, *Adv. Funct. Mater.* **2014**, *24*, 7681.

[22] K. Sivula, F. Le Formal, M. Gratzel, *Chem. Mater.* **2009**, *21*, 2862.

[23] T. Hisatomi, H. Dotan, M. Stefik, K. Sivula, A. Rothschild, M. Gratzel, N. Mathews, *Adv. Mater.* **2012**, *24*, 2699.

[24] T. Hisatomi, J. Brillet, M. Cornuz, F. LeFormal, N. Tetreault, K. Sivula, M. Gratzel, *Faraday Discuss.* **2012**, *155*, 223.

[25] O. Zandi, J. A. Beardslee, T. Hamann, *J. Phys. Chem. C* **2014**, *118*, 16494.

[26] M. J. Kang, Y. S. Kang, *J. Mater. Chem. A* **2015**, *3*, 15723.

[27] A. Kay, I. Cesar, M. Gratzel, *J. Am. Chem. Soc.* **2006**, *128*, 15714.

[28] S. D. Tilley, M. Cornuz, K. Sivula, M. Gratzel, *Angew. Chem., Int. Ed.* **2010**, *49*, 6405.

[29] F. Le Formal, M. Gratzel, K. Sivula, *Adv. Funct. Mater.* **2010**, *20*, 1099.

[30] Y. Q. Liang, C. S. Enache, R. van de Krol, *Int. J. Photoenergy* **2008**, 739864, https://doi.org/10.1155/2008/739864.

[31] D. Wang, X.-T. Zhang, P.-P. Sun, S. Lu, L.-L. Wang, Y.-A. Wei, Y.-C. Liu, *Int. J. Hydrogen Energy* **2014**, *39*, 16212.

[32] C. Zhang, Q. W. Wu, X. Ke, J. Wang, X. Jin, S. Xue, *Int. J. Hydrogen Energy* **2014**, *39*, 14604.

[33] S. H. Shen, S. A. Lindley, X. Y. Chen, J. Z. Zhang, *Energy Environ. Sci.* **2016**, *9*, 2744.

[34] P. S. Shinde, S. Y. Lee, S. H. Choi, H. H. Lee, J. Ryu, J. S. Jang, *Sci. Rep.* **2016**, *6*, 32436.

[35] S. Mathur, M. Veith, V. Sivakov, H. Shen, V. Huch, U. Hartmann, H.-B. Gao, *Chem. Vap. Deposition* **2002**, *8*, 277.

[36] X. D. Wen, R. L. Martin, G. E. Scuseria, S. P. Rudin, E. R. Batista, A. K. Burrell, *J. Phys.: Condens. Matter* **2013**, *25*, 025501.

[37] E. S. Ilton, J. F. Boily, P. S. Bagus, *Surf. Sci.* **2007**, *601*, 908.

[38] D. W. Shoesmith, *J. Nucl. Mater.* **2000**, *282*, 1.

[39] M. Barroso, S. R. Pendlebury, A. J. Cowan, J. R. Durrant, *Chem. Sci.* **2013**, *4*, 2724.

[40] A. G. Tamirat, J. Rick, A. A. Dubale, W. N. Su, B. J. Hwang, *Nanoscale Horiz.* **2016**, *1*, 243.

[41] M. Pyeon, T.-P. Ruoko, Y. Gonullu, M. Deo, N. V. Tkachenko, S. Mathur, *J. Mater. Res.* **2018**, *33*, 455.

[42] A. Rohrbach, J. Hafner, G. Kresse, *Phys. Rev. B* **2004**, *70*, 125426.

[43] S. H. Shen, J. Zhou, C.-L. Dong, Y. Hu, E. N. Tseng, P. Guo, L. Guo, S. S. Mao, *Sci. Rep.* **2014**, *4*, 6627.

[44] J. G. Chen, *Surf. Sci. Rep.* **1997**, *30*, 1.

[45] J. Suntivich, K. J. May, H. A. Gasteiger, J. B. Goodenough, Y. A. Shao-Horn, *Science* **2011**, *334*, 1383.

[46] J. Suntivich, W. T. Hong, Y.-L. Lee, J. M. Rondinelli, W. Yang, J. B. Goodenough, B. Dabrowski, J. W. Freeland, Y. S. Horn, *J. Phys. Chem. C* **2014**, *118*, 1856.

[47] X.-D. Wen, M. W. Loble, E. R. Batista, E. Bauer, K. S. Boland, A. K. Burrell, S. D. Conradson, S. R. Daly, S. A. Kozimor, S. G. Minasian, R. L. Martin, T. M. McCleskey, B. L. Scott, D. K. Shuh, T. Tyliszczak, *J. Electron Spectrosc. Relat. Phenom.* **2014**, *194*, 81.

[48] T. P. Ruoko, K. Kaunisto, M. Bartsch, J. Pohjola, A. Hiltunen, M. Niederberger, N. V. Tkachenko, H. Lemmetyinen, *J. Phys. Chem. Lett.* **2015**, *6*, 2859.

[49] S. Sorenson, E. Driscoll, S. Haghighat, J. M. Dawlaty, *J. Phys. Chem. C* **2014**, *118*, 23621.

[50] P. E. Blochl, *Phys. Rev. B* **1994**, *50*, 17953.

[51] G. Kresse, D. Joubert, *Phys. Rev. B* **1999**, *59*, 1758.

[52] G. Kresse, J. Furthmuller, *Phys. Rev. B* **1996**, *54*, 11169.

[53] X. D. Wen, R. L. Martin, G. E. Scuseria, S. P. Rudin, E. R. Batista, T. M. McCleskey, B. L. Scott, E. Bauer, J. J. Joyce, T. Durakiewicz, *J. Chem. Phys.* **2012**, *137*, 154707.

[54] G. Rollmann, A. Rohrbach, P. Entel, J. Hafner, *Phys. Rev. B* **2004**, *69*, 165107.